CDF/ANAL/JET/CDFR/6298
Version 2.2

First Measurement of the Inclusive Jet Cross Section in Run II

F. Chlebana, G. Flanagan,

A. Bhatti, J. Dittmann, J. Huston, G. Latino, M. Martinez-Perez, R. Snihur

March 21, 2003

Abstract

This note describes the measurement of the inclusive jet cross section in Run II based on 85.3 pb^{-1} of data collected from February 9, 2002 to January 9, 2003. Jets in the data span the E_T range from 44–550 GeV, extending the Run I upper limit by almost 150 GeV. The results are compared to NLO QCD predictions using the CTEQ6.1 PDF set.

1 Introduction

Jet production at the Tevatron probes the highest momentum transfer region currently accessible and thus is potentially sensitive to a wide variety of new physics. There was great interest when the inclusive jet cross section measured by CDF in Run I exhibited an excess at high jet E_T using then-current parton distribution functions. Global PDF analyses by CTEQ [1, 2] have demonstrated that one explanation for the excess at high E_T is a larger-than-expected gluon distribution at high x. The gluon distribution at high x has indeed increased in recent PDF fits (CTEQ6, CTEQ6.1) [3, 4], leading to better agreement with both the CDF and D0 inclusive jet cross section measurements. However, a great deal of uncertainty on the gluon distribution at high x still remains.

The increase in the center-of-mass energy from 1.8 TeV to 1.96 TeV and the large integrated luminosity expected of Run II will dramatically increase the kinematic range for measuring jet production and the potential for discovering new physics. With a Run II data sample similar in size to that obtained in Run Ib, we are already able to measure jet production at transverse energies far beyond those possible in Run I.

This analysis is restricted to the central rapidity region used in previous CDF inclusive jet publications, although future analyses will also examine the inclusive jet cross section in the forward rapidity regions. Extending the measurement beyond the central region provides a powerful way to distinguish between conventional and non-conventional explanations for any cross section excess in the central region [3].

In order to obtain first results in a timely fashion, we have utilized the same techniques used in the previous CDF Run I inclusive jet analysis [5]. In particular, we apply the Run I jet algorithm (JETCLU, cone $R = 0.7$) for the results quoted in this note. Upcoming analyses will use the standard Run II jet algorithms. Also, we currently rely on the absolute jet energy corrections determined in Run I; the jet energy scale has been set to that of Run I by tuning the photon + jet p_T balance, as discussed in Section 4.

2 Data Sample and Analysis Cuts

Data collected from February 9, 2002 (run 138815) through January 9, 2003 (run 156369) are used in this analysis. The data were written to the `gjet08` dataset which was processed with version 4.8.4 of the offline software. The data were later reprocessed with version 4.9.1 of the offline software and written out into ntuples. There are about 107 pb^{-1} of data written to tape in the run range considered. After applying good run criteria (see Section 2.2) the data sample was reduced to 85.3 pb^{-1}.

Prior to February 9, 2002, jet triggers were written to the `gtst1c` and `gtst1d` datasets. For these early datasets there were changes to the online calibration of the calorimeter, and for simplicity we do not include them in this analysis.

Dataset	Integrated luminosity (nb^{-1})
`gtst1c`	3429
`gtst1d`	1820
`gjet08` (all)	107231
`gjet08` (good runs)	85348

Table 1: The total integrated luminosity for datasets with jet triggers.

2.1 Trigger Paths

The data were collected using the four different trigger paths listed in Table 2. The prescales for each trigger are given in parentheses.

The Level 1 trigger consisted of a single tower in the calorimeter with a threshold of 5 GeV (ST5) having a prescale of 20 and a second threshold of 10 GeV (ST10)

L1 Trigger	L2 Trigger	L3 Trigger
ST5 (20)	CL15 (12, 25)	J20
	CL40 (1)	J50
ST10 (1)	CL60 (8)	J70
	CL90 (1)	J100

Table 2: The trigger paths and prescales (in parentheses).

with a prescale of 1. There are four Level 2 triggers which use calorimeter cluster information with thresholds of 15, 40, 60 and 90 GeV (CL15, CL40, CL60 and CL90). The lower-threshold Level 2 triggers (CL15 and CL40) require that the Level 1 ST5 trigger fired while the CL60 and CL90 triggers require ST10. The prescale on the CL15 trigger was changed from 12 to 25 starting with run 153067. The Level 3 triggers use the JETCLU algorithm to reconstruct jets with a cone size $R = 0.7$. The event vertex for jet reconstruction at Level 3 is $z = 0$. No prescales are applied at Level 3 and the jet thresholds are 20, 50, 70 and 100 GeV.

Since the prescale of the C15 trigger changed from 12 to 25 beginning with run 153067, we must determine the effective prescale for the set of runs included in this analysis. The effective prescales for ST5, CL15, and CL60 can be determined directly from the data using trigger information stored in the event record. For events collected on an independent trigger, one can divide the number of events that fired a particular trigger by those that were accepted after prescaling to obtain the effective prescale. The results using this method ("Method 1") are summarized in Table 3. The final inclusive jet cross section is calculated using these effective prescales.

Trigger	Fired	Accepted	Effective prescale
ST5	1.50833E+06	75558	19.96 ± 0.07
C15	1.5264E+06	98088	15.56 ± 0.05
C60	1.32131E+06	164907	8.01 ± 0.02

Table 3: The effective prescale of the main triggers as determined from the data (Method 1).

As a crosscheck, Figure 1 shows the number of events in the J100 sample divided by the number of events passing the J70, J50, and J20 triggers after prescaling as a function of Level 3 jet E_T (for $E_T > 100$ GeV). Measurements of the effective prescales are obtained by fitting a straight line to the ratios (Method 2). The results are in agreement with those obtained by Method 1, as shown in Table 4.

The raw inclusive jet E_T distribution is shown in Figure 2 after correcting for the effective prescales determined using Method 1.

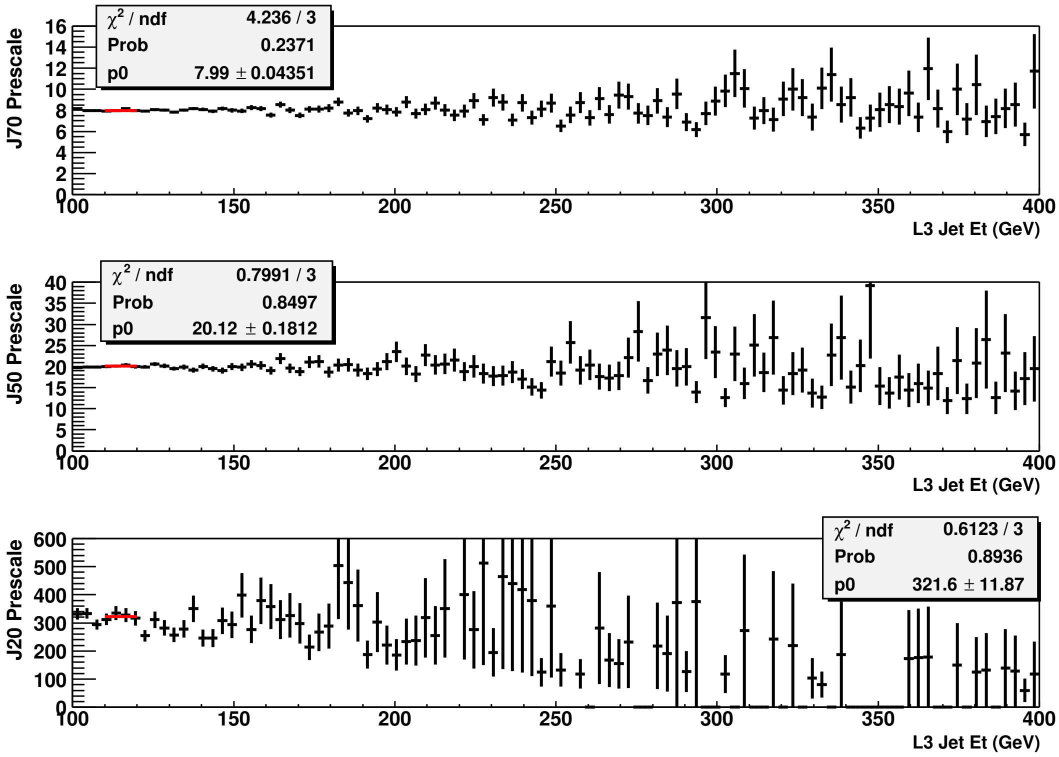

Figure 1: As a function of Level 3 jet E_T ($E_T > 100$ GeV), the number of events that pass the J100 trigger divided by the number of events that pass the J70 (top), J50 (middle) and J20 (bottom) triggers after prescaling.

Trigger	Prescale	
	Method 1	Method 2
J20	311.61 ± 0.02	321 ± 12
J50	19.95 ± 0.07	20.12 ± 0.18
J70	8.01 ± 0.02	7.99 ± 0.04
J100	1	1

Table 4: The effective prescales determined from trigger information in the event record (Method 1) and from the number of events in the J100 sample that pass the J20, J50 and J70 triggers (Method 2).

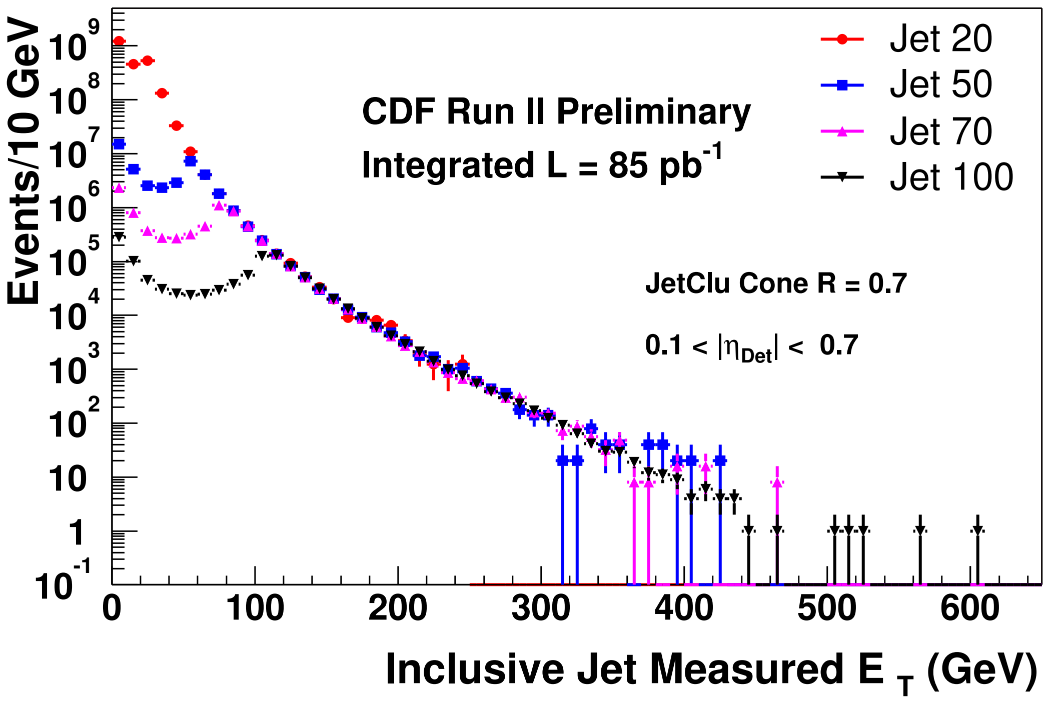

Figure 2: The raw inclusive jet E_T distribution for the four jet triggers after correcting for the prescales.

2.2 Good Run Criteria

Runs are required to pass the "good run" criteria. A good run list is composed by querying the database with the following requirements:

```
SHIFTCREW_STATUS  = 1
RUNCONTROL_STATUS = 1
OFFLINE_STATUS    = 1
RUNNUMBER  >= 138815
CLC_STATUS  = 1
L1T_STATUS  = 1
L2T_STATUS  = 1
L3T_STATUS  = 1
CAL_STATUS  = 1
CAL_OFFLINE = 1
(COT_STATUS = 1 OR COT_OFFLINE = 1)
```

In addition, there is a check to make sure that the number of events in the ntuple is identical to the number of events recorded in the database. This additional requirement removes 31 runs with a total luminosity of 5 pb^{-1}. The lost runs are listed in Table 5.

Run	N events (database)	N events (ntuple)	Run	N events (database)	N events (ntuple)
144624	4182	0	155129	22666	22110
144627	2238	1365	155764	1173	586
145415	1229	1287	156362	2773	2267
150145	716	4638	156365	1395	0
150803	30016	28638	156369	11538	0
151435	8140	6987	156370	728	0
151683	11523	12833	156371	1383	0
151900	8020	7162	156455	3594	0
152944	3073	1317	156372	1111	0
152967	47877	46016	156401	2643	0
153411	2083	1023	156452	1422	0
153416	23629	22754	156454	1788	0
153446	5802	4702	156457	3374	0
154050	30955	29997	156458	5178	0
154208	18590	18038	156460	14854	0
			156464	1988	52

Table 5: List of runs for which there is a discrepancy between the number of J20 events recorded in the database and the number found in the ntuple.

Run 138815, recorded on February 9, 2002, is the first run where the online shift crew determined that the subdetector components were all functioning properly. There are approximately 7 pb^{-1} of processed data before run 138815; however, only $\sim$30 nb^{-1} would satisfy the other criteria.

The online check of the calorimeter system ensures the electronics were working properly (no new dead channels, and no sets of 12 or more consecutive dead channels). The offline check of the calorimeter system requires no COLD or HOT calorimeter towers that cannot be fixed with offline code. A "COLD" tower is a tower which records hits less frequently that it is supposed to. The ultimate COLD tower is a "DEAD" tower, meaning that it records nothing. A "HOT" tower is a tower that records hits too often.

Up to the Tevatron shutdown in January 2003, these requirements were satisfied by 685 runs, with a total offline luminosity of 90.1 pb^{-1}.

2.3 Event Selection

Events are required to pass the cuts listed in Table 6.

Cut	Events remaining			
	J20	J50	J70	J100
Full sample	5607610	1477696	678921	856961
$0.1 < \|\eta_D\| < 0.7$	495149	680304	349944	444465
$\|z\| \leq 60$ cm	473676	638966	328096	417181
$\widetilde{\not\!\!E_T} \leq$ X	471761	631694	319203	383402
$E_{tot} \leq 2000$ GeV	471761	631694	319203	383399
Hadron timing	469434	624365	313366	372146

Table 6: List of selection cuts with the number of events remaining after each successive cut. The cut on E_{tot} was ultimately reduced to 1500 GeV to reduce the background from cosmic showers (see text). In this analysis the hadron timing cut is not applied.

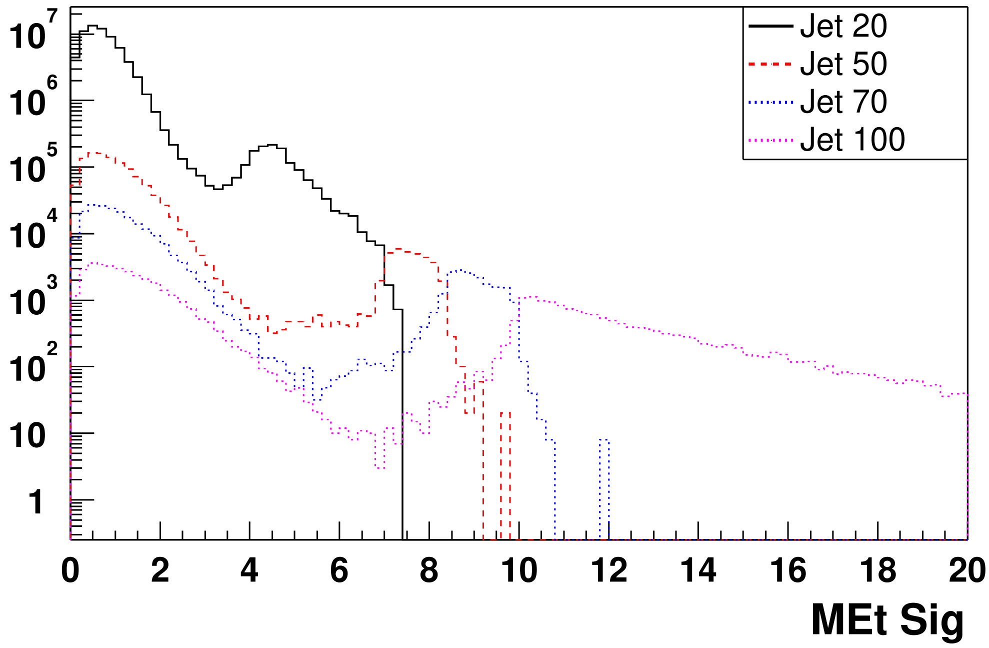

Figure 3: The missing E_T significance ($\widetilde{\not\!\!E_T}$) distribution for the four different jet triggers. As the E_T of the sample increases, the second peak shifts to higher values.

The missing E_T significance, defined as $\widetilde{\not\!\!E_T} = \not\!\!E_T/\sqrt{\sum E_T}$, is plotted in Figure 3 for the four jet triggers. The second peak moves to higher values as the the jet E_T threshold increases. In order to accommodate this we have applied a sliding $\widetilde{\not\!\!E_T}$ cut for the different jet triggers. For J20, J50, J70 and J100 the cut used is 3.5, 5.0, 6.0 and 7.0, respectively.

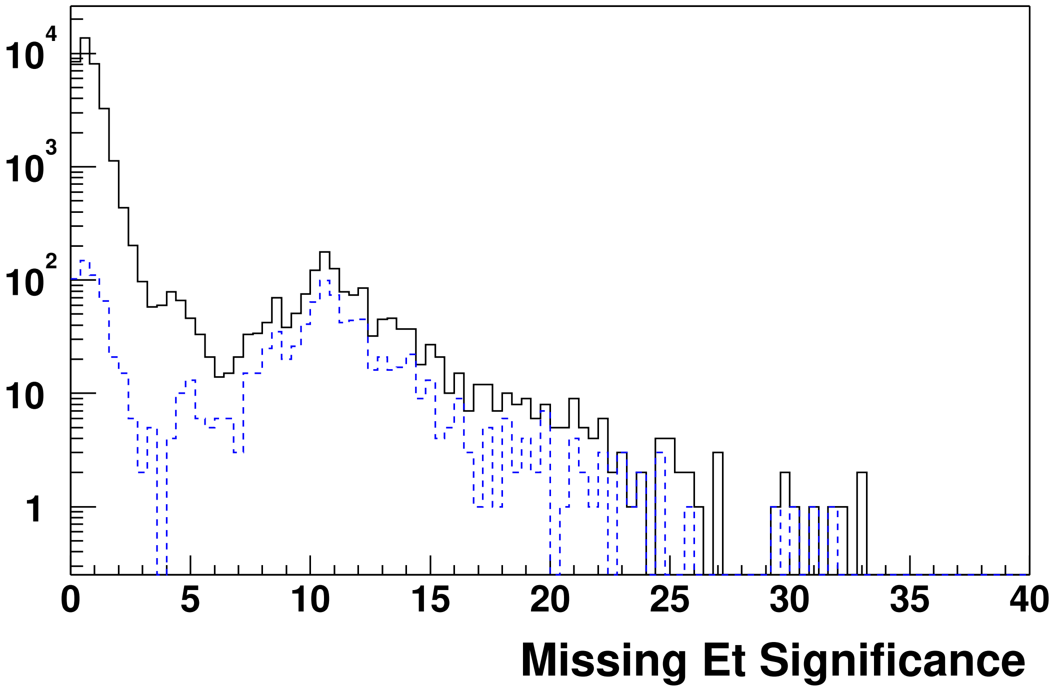

Figure 4: Events tagged having out-of-time energy are shown in the dashed histogram.

Trigger	Fraction
J20	0.995
J50	0.988
J70	0.982
J100	0.971

Table 7: Fraction of events that survive the hadron timing requirement after all other cuts are applied.

The hadron timing filter [7] was examined as a way to reject potential cosmic ray events. The $\widetilde{\not{E}_T}$ distribution of events that are tagged as cosmic rays by out-of-time energy are shown in Figure 4 (dashed histogram).

Most background from cosmic ray events are rejected by the $\widetilde{\not{E}_T}$ cut and at this time we do not apply the hadron timing cut. As shown in Table 7, the fraction of events rejected by the hadron timing cut increases from 0.5% to 3% as the jet E_T increases. We note that the number of jets in the two highest E_T bins are unaffected by the hadron timing cut. Further studies of this cut will be done before it will be used.

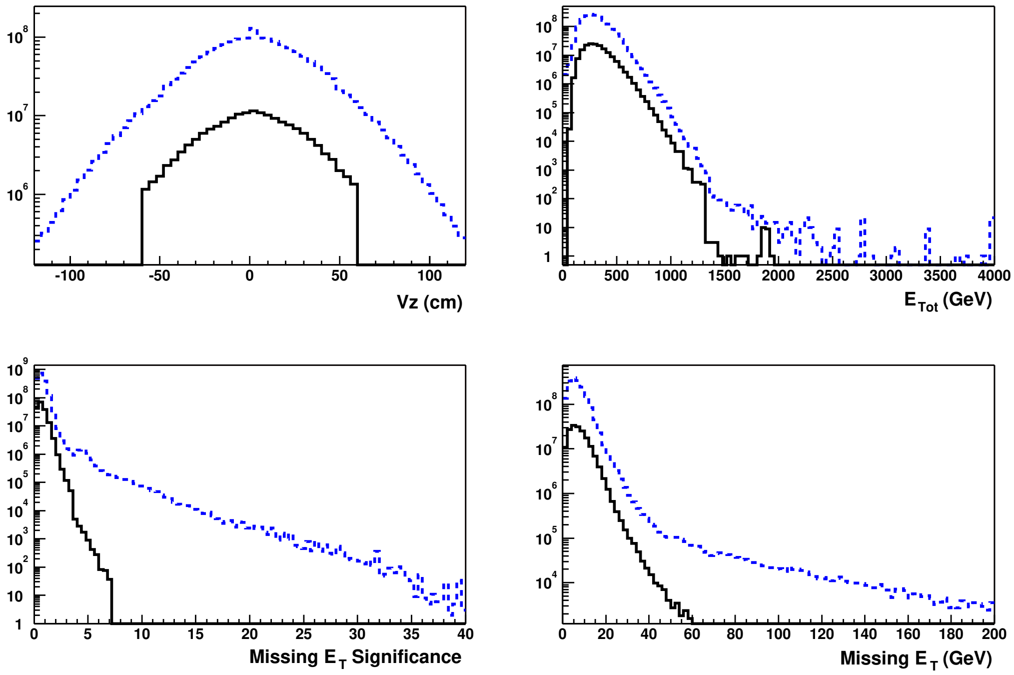

Figure 5: Global distributions of the event sample before (dashed lines) and after (solid lines) the selection cuts are applied. The $E_{tot} \leq 2000$ GeV cut was used for the upper-right plot; the cut was later changed to $E_{tot} \leq 1500$ GeV (see text).

Figures 5 and 6 show some global distributions of the events before and after the selection cuts are applied. The lead jet ϕ distribution shown in Figure 6 shows an enhancement at $\phi = 0$ and around $\phi = 1.8$. These effects are currently being studied.

The events clustered at high E_{tot} are background from cosmic showers. In order to reduce this background the E_{tot} cut was lowered from 2000 to 1500 GeV. This removed one background event in the third-highest E_T bin, reducing the bin content from 70 to 69 events. There were no events removed in the highest two E_T bins.

2.4 Vertex Efficiency

In order to ensure a good energy measurement of jets, the event vertex is required to be within 60 cm of the center of the detector along the beam direction. This cut accepts 95% of the events. Table 8 lists the number of events that pass the vertex requirement. A correction factor of 5% is applied to the data to account for events removed by the vertex requirement. Prior to the vertex cut, all other cuts are applied. The result of 5% is consistent with the vertex efficiency determined in a separate study using the minimum bias data sample [6].

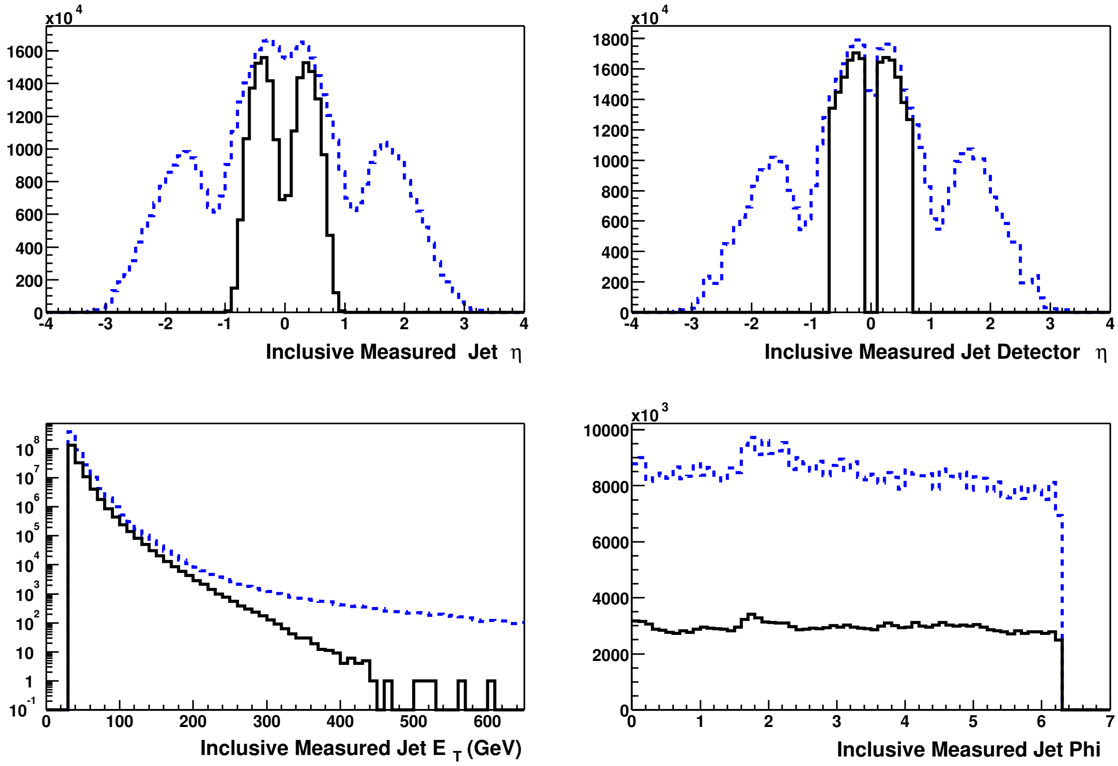

Figure 6: Global distributions of the event sample before (dashed lines) and after (solid lines) the selection cuts have been applied.

Trigger	Failed	Passed	(F+P)/P
J20	13676	271365	1.0504
J50	41875	734942	1.05698
J70	23540	378183	1.06225
J100	30837	469435	1.06569

Table 8: The number of events passing all selection cuts including the vertex cut ("Passed"). Events failing the vertex cut after all other selection cuts ("Failed").

3 Trigger Efficiency

The trigger efficiency of the four jet triggers as a function of inclusive jet E_T (after production) is shown in Figure 7. Jets are reconstructed using JETCLU with a cone size of $R = 0.7$.

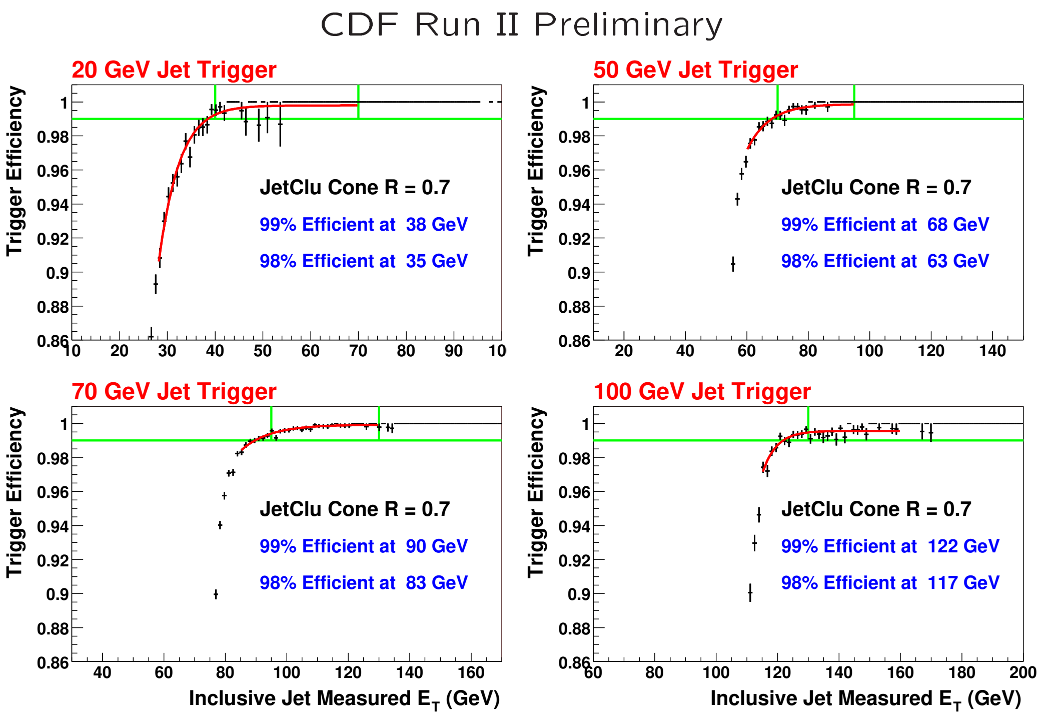

Figure 7: The trigger efficiency as a function of inclusive jet E_T for the four jet trigger thresholds.

For each trigger we use a lower-threshold sample in order to determine the trigger efficiency, *e.g.* the ST5 sample is used to measure the J20 trigger efficiency and the J20 sample is used to measure the J50 trigger efficiency. Efficiency curves of the form

$$eff(x) = \frac{P_0}{1 + \exp\left[(-P_1 \cdot (x + P_2)\right]} \tag{1}$$

are fit to the data. P_0, P_1 and P_2 are determined from the fit. Table 9 list the results of fit for the four jet triggers.

The results were obtained after applying the 4.2% energy scale correction to the jets (see Section 4). The bin boundaries used in this analysis, listed in Table 10, are well away from the trigger thresholds and in a region where the trigger is above 99% efficient.

Trigger	P_0	P_1	P_2
J20	0.9979	0.247	18.94
J50	0.9987	0.141	34.75
J70	0.9993	0.108	45.40
J100	0.9956	0.222	98.59

Table 9: The parameters determined by fitting the trigger efficiency.

Trigger	Min (GeV)	Max (GeV)
J20	40	70
J50	70	95
J70	95	130
J100	130	

Table 10: The bin boundaries used for the different trigger samples.

Trigger	Inclusive Jet E_T 98% Efficiency (GeV)	Inclusive Jet E_T 99% Efficiency (GeV)
J20	35	38
J50	62	68
J70	83	90
J100	117	122

Table 11: The JETCLU jet E_T for each trigger for 98% and 99% efficiencies.

4 Run II-Run I Jet Energy Scale

Using the Run I unsmearing procedures for Run II data requires the raw energy scale for central jets to be the same.

A Run II-Run I central ($0.2 < |\eta_D| < 0.8$) jet energy scale comparison has been performed by studying γ-jet balancing in events from inclusive photon triggers [8]. The jet energy response is lower in Run II than it is in Run I. For cone jets with $R = 0.7$, we observe a 3% difference in the mean value of the γ-jet balancing function defined by:

$$f_b = \frac{{P_T}^{jet}(\text{raw}) - {P_T}^{\gamma}}{{P_T}^{\gamma}} \tag{2}$$

The difference, as shown in Figure 8, corresponds to a 1.042 Run II-Run I rescaling correction factor in the raw jet energy scale as given by the following relation:

$$K_J = \frac{< f_b(\text{Run I}) > +1}{< f_b(\text{Run II}) > +1} \tag{3}$$

where K_J is defined by

$$< P_T^J(\text{Run I}) > \; = \; K_J \; < P_T^J(\text{Run II}) > . \tag{4}$$

Similar results, within errors, are found for cone 0.4 and cone 1.0 jets.

The origin of this difference in jet energy scale is still an open question. The Run I and Run II γ-jet data samples were selected according to the same selection criteria (detailed in Ref. [8]) in order to make the two analyses as similar as possible. In particular, proper CEM and CHA energy scale corrections were respectively applied to the electromagnetic and hadronic fractions of the jet energy in order to account for low calorimeter response observed in both Run I and Run II data.

Updated results obtained with optimized offline calorimeter corrections (version 4.9.1) are consistent with the measurements quoted here. Also, as shown in Figure 9, no indication of a dependence of the rescaling factor K_J on the jet energy scale was observed in the kinematic range accessible with the γ-jet data sample (up to 75 GeV). *Consequently, we have decided to assign a 5% uncertainty to the Run II raw jet energy scale after applying the rescaling factor.*

These results are consistent with an independent check on the Run II jet energy scale in the dijet cross section analysis [9]. In that analysis, after the 1.042 Run II-Run I rescaling factor is applied, the ratio of the measured Run II to Run I cross sections agree reasonably well with LO QCD predictions to within roughly 10% in rate, corresponding to ~2% in jet energy scale. This supports the fact that the Run II jet energy scale is lower than that of Run I by roughly the same amount (within the quoted systematics) as the rescaling factor found from γ-jet balancing.

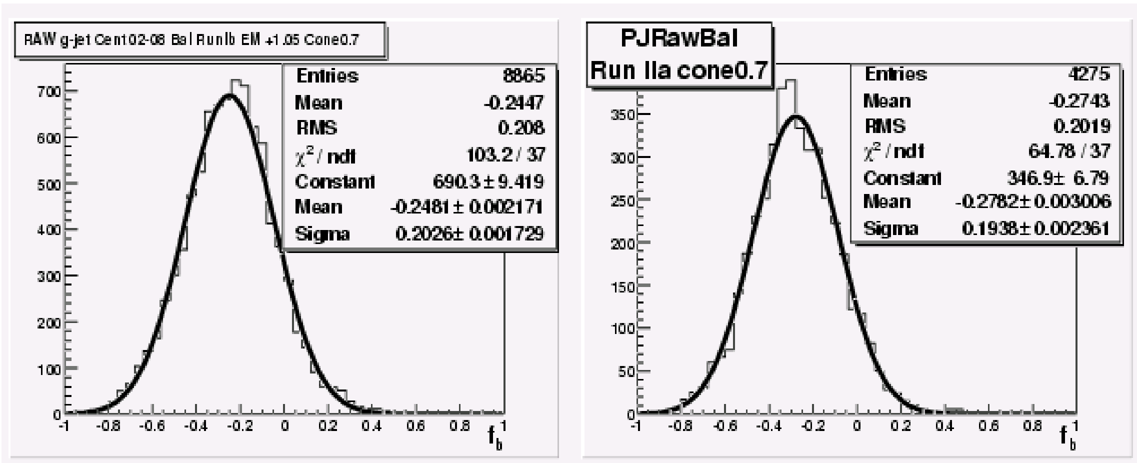

Figure 8: Gaussian fit for the f_b function (defined by Equation 2) for cone 0.7 jets in Run I (left) and Run II (right) data. Raw jets with $0.2 < |\eta_D| < 0.8$ have been considered.

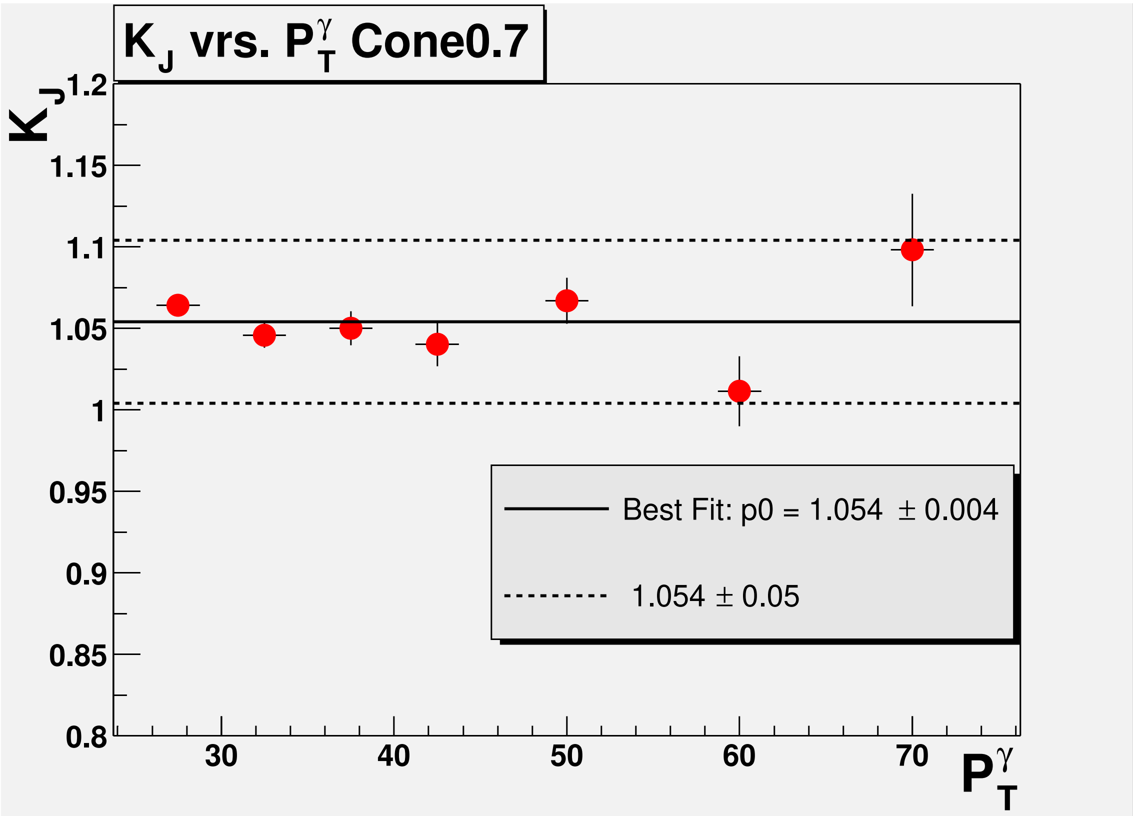

Figure 9: Run II-Run I jet energy rescaling factor K_J (defined by Equation 3) as a function of the jet energy scale, parametrized by P_T^γ. The best fit to the data points (solid line) is a constant whose value (1.054) is consistent, within errors, with the one applied to the data (1.042). High p_T bins (characterized by a very reduced statistics) have values fluctuating within the ± 5% quoted systematic uncertainty (dashed lines). Cone 0.7 raw jets with $0.2 < |\eta_D| < 0.8$ have been considered.

5 Calorimeter Energy Corrections

Version 4.9.1 of the offline code has incorporated additional calorimeter energy corrections. A correction to the CEM LERs (Linear Energy Response constants) was applied in offline processing to all runs taken before the June 2002 shutdown; for subsequent runs, these corrections are applied online. Similarly, a 4% correction for the CHA LERs is applied offline (online) before (after) October 2, 2002, corresponding to run 152400. The CEM energy scale exhibited a time dependence on the order of 3% between February–September 2002, and this dependence was corrected for using the offline SCL constants. After run 152400, the CEM scale was shifted upward by 3%, and no correction was applied offline. The original reconstructed banks were dropped from the data and calorimetry was redone. The *tcl* fragments used in the reprocessing are listed below.

```
talk DHInput
  dropList set CdfJetColl CdfMet CalData
  dropList add CdfMuonColl
  dropList add CdfEmClusterColl CdfEmObjectColl
  dropList add Pi0CandidateCollection CdfTauCollection

mod enable CalorimetryModule
mod talk CalorimetryModule
  useOffScl       set true
  makeOfflineLers set true
  createCalData   set true
  verbose set f
exit

mod talk CdfMetModule
 parmSetName set QCD
 vertexStrategy set 1
 show
exit

mod talk JetCluModule-cone0.7PrimVertex
 parmSetName set QCD
 vertexStrategy set 1
 coneRadius set 0.7
 show
exit
```

6 Unsmearing Procedure

The raw cross section is determined using the equation

$$\sigma_i^{\rm raw} = \frac{N_i}{\Delta E_{Ti}\,\Delta\eta_D\,L} \tag{5}$$

where N_i is the number of events in bin i, ΔE_{Ti} is the bin width in E_T, $\Delta\eta_D = 1.2$ is the η_D width, and L is the effective integrated luminosity accounting for the prescales.[1] The raw cross sections are then input to the same unsmearing procedure used in Run I. The physics function is given in Equation 6 and the results of the fit are listed in Table 12.

$$\text{physFun}(E_T) = p_0 \times \left[1 - \frac{2E_T}{1960}\right]^{p_6} \times \text{pow}\left[10, \sum_{n=1}^{5} p_n[\log(E_T)]^n\right] \tag{6}$$

For 35 data points the total χ^2 is 44.5 and the χ^2/dof is 1.59. The data are compared to the fit in Figure 10, and the residuals are plotted in Figure 11.

[1] Values of L in this note are not yet corrected for the +1.9% increase introduced at the Joint Physics Meeting on February 21, 2003.

p_0	p_1	p_2	p_3	p_4	p_5	p_6
0.23892E+06	−2.3859	4.6578	−5.0552	1.7446	−0.2070	7.0888

Table 12: The parameters of the physics function fit to the unsmeared inclusive jet E_T distribution.

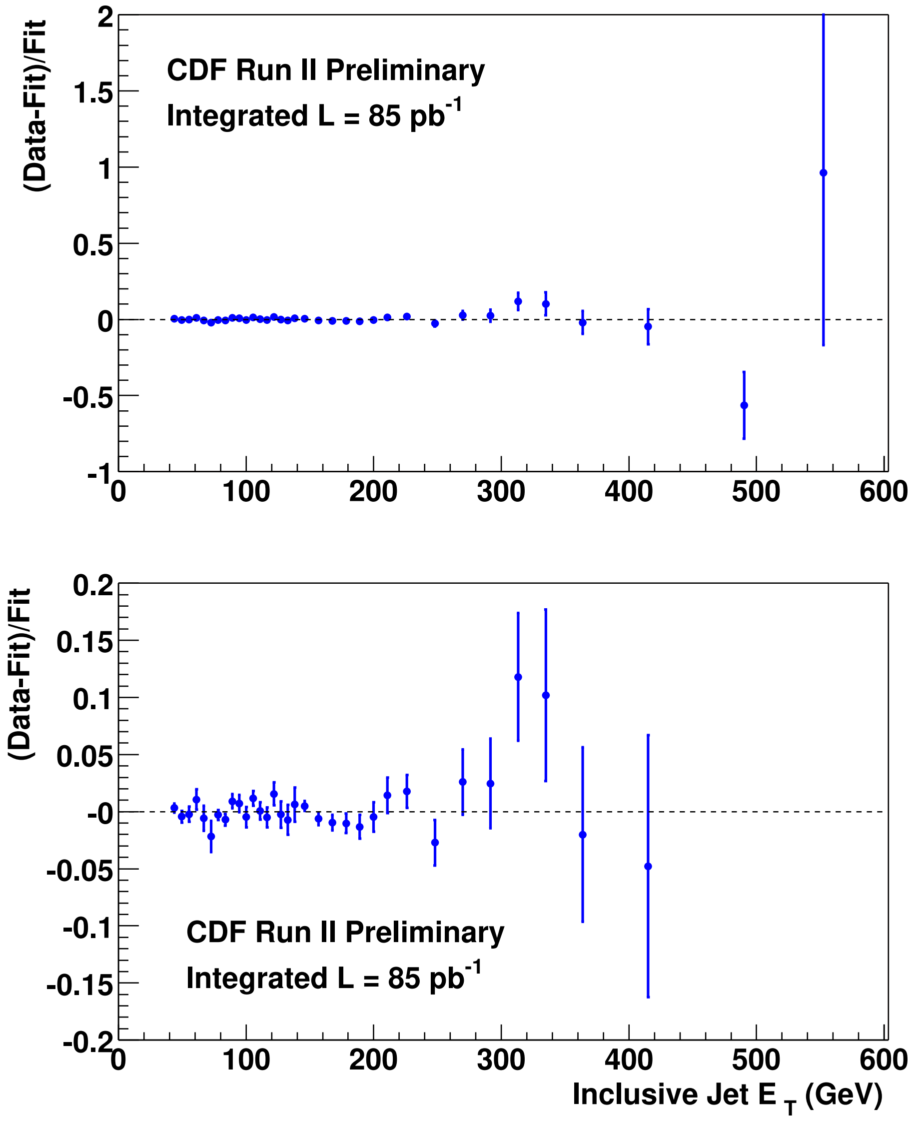

Figure 10: (Data - fit)/fit is plotted as a function of the inclusive jet E_T.

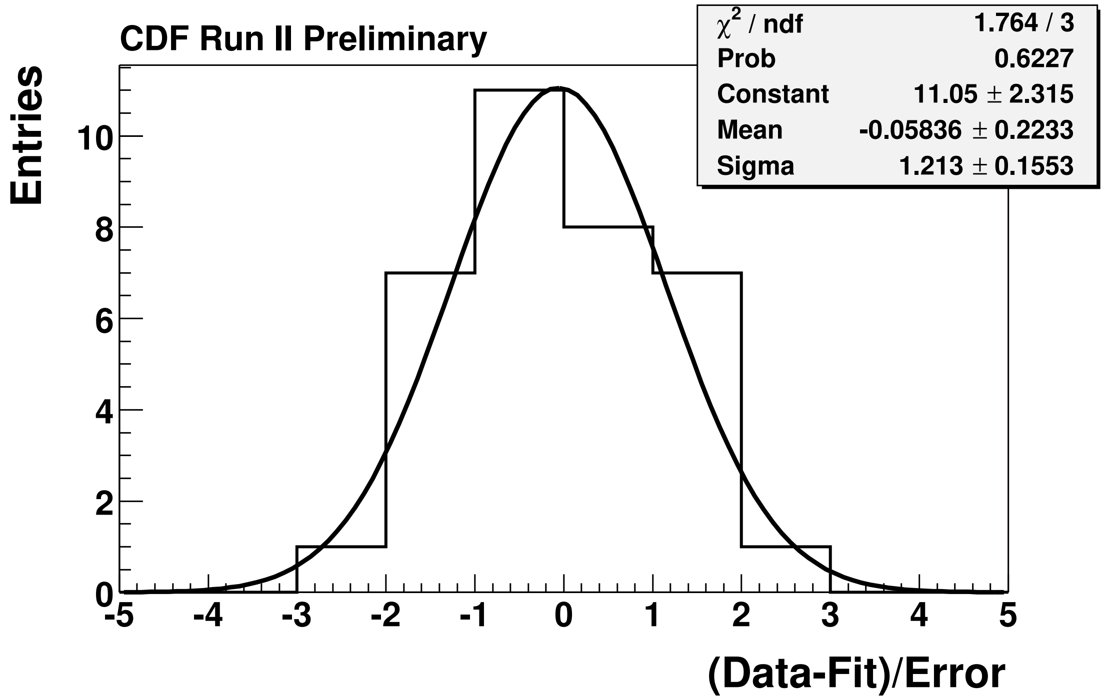

Figure 11: The residuals of the physics function fit to the data.

7 Jet η_J vs. η_D

The fit to the cross section using the cut $0.1 < \eta_J < 0.7$ (where η_J is calculated using the reconstructed event vertex) is compared to the result when using $0.1 < \eta_D < 0.7$ (where η_D is calculated using $z = 0$) in Figure 12, where the ratio of the physics functions is plotted. A comparison of the raw number of events in the highest E_T bins using η_J and η_D is shown in Table 13.

Bin edges		Jet η_J		Jet η_D	
low E_T (GeV)	high E_T (GeV)	$< E_T >$ (GeV)	N events	$< E_T >$ (GeV)	N events
300	320	309.08	214	309.11	216
320	360	336.28	171	336.06	165
360	440	386.27	70	387.97	70
440	520	479.86	5	484.86	4
520	620	574.55	3	568.29	3

Table 13: The raw number of events in the highest E_T bins when using jet η_J and jet η_D.

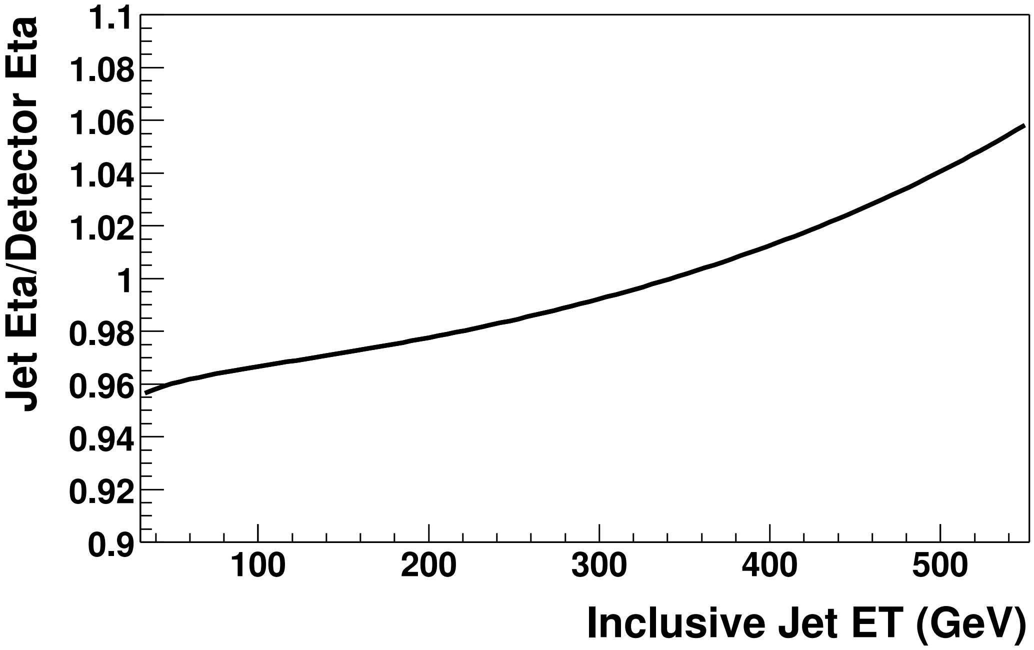

Figure 12: The ratio of the physics function determined using jet η_J to that determined using jet η_D.

8 Systematic Uncertainty

The jet systematic uncertainties are assumed to have the same values as measured in Run I, with the exception of an additional energy scale uncertainty due to the correction determined by photon-jet balancing. The systematic errors arise from seven separate sources. The percent uncertainty on the jet cross section associated with each source is evaluated through shifts to the response function. Each source of systematic error is varied by one sigma, and the modified response functions are then used to repeat the unsmearing procedure to find the modified physics function. The difference between the modified physics function and the nominal physics function corresponds to a one-sigma uncertainty. The following sources of systematic errors are considered:

- "Hi p_T": High p_T hadronic response +3.2% –2.2%.
- "Lo p_T": Low p_T hadronic response $\pm$5%.
- "E scale": Energy scale stability $\pm$5.0%.
- "Frag": Fragmentation.

- "UE": Underlying event ±30%.
- "Ele/pho": Electron/photon response ±2%.
- "Res": Calorimeter resolution ±10%.

In Run I, the systematic uncertainties were found by calculating the difference between the central physics function and the physics function determined for a particular source of systematic error. However, the freedom at high E_T, together with the large statistical error, can lead to a large apparent deviation. This effect is shown in Figure 13, where the dashed line shows the difference between the physics functions, the symbols show the difference between the corrected data points, and the solid lines show a third-order polynomial fit to the points. For this reason we choose to use the polynomial fit to represent the 5% energy scale uncertainty. For the other sources of uncertainty we use the difference in the physics functions (Sys P − Sys N)/2 for both the positive and negative uncertainties. Once we have more statistics we can examine the systematic uncertainties with greater precision.

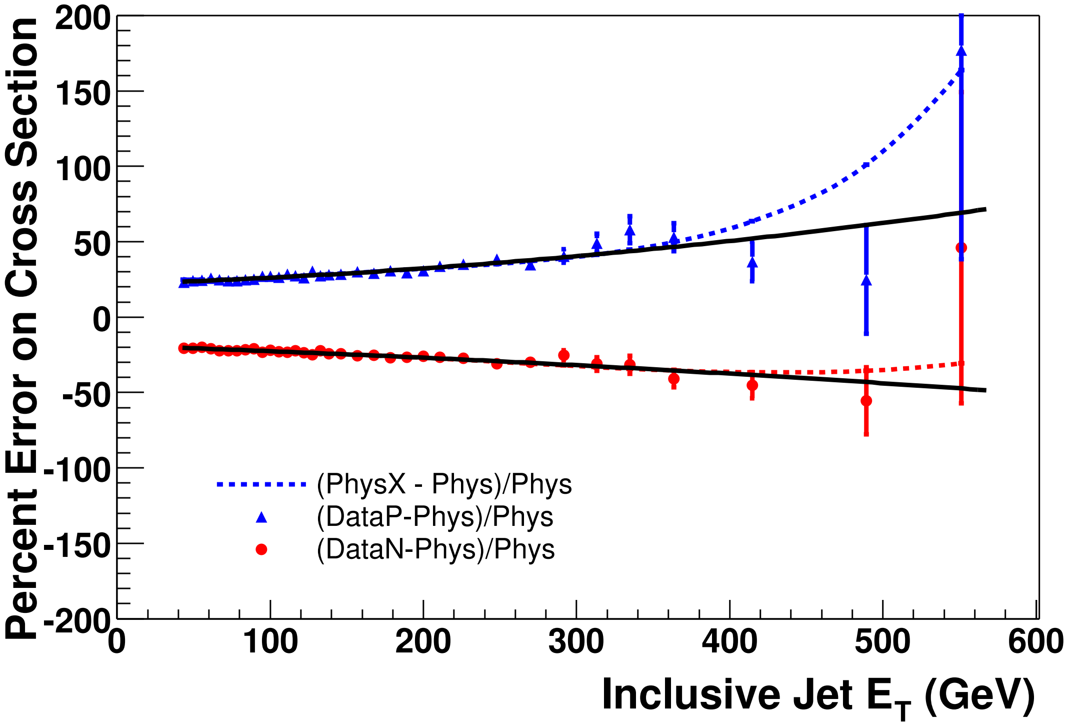

Figure 13: The percent error on the corrected cross section corresponding to the energy scale uncertainty. The dashed line shows the shift when comparing the physics functions. The points are the actual shift in the corrected cross section. The solid line is the result of a polynomial fit to the points.

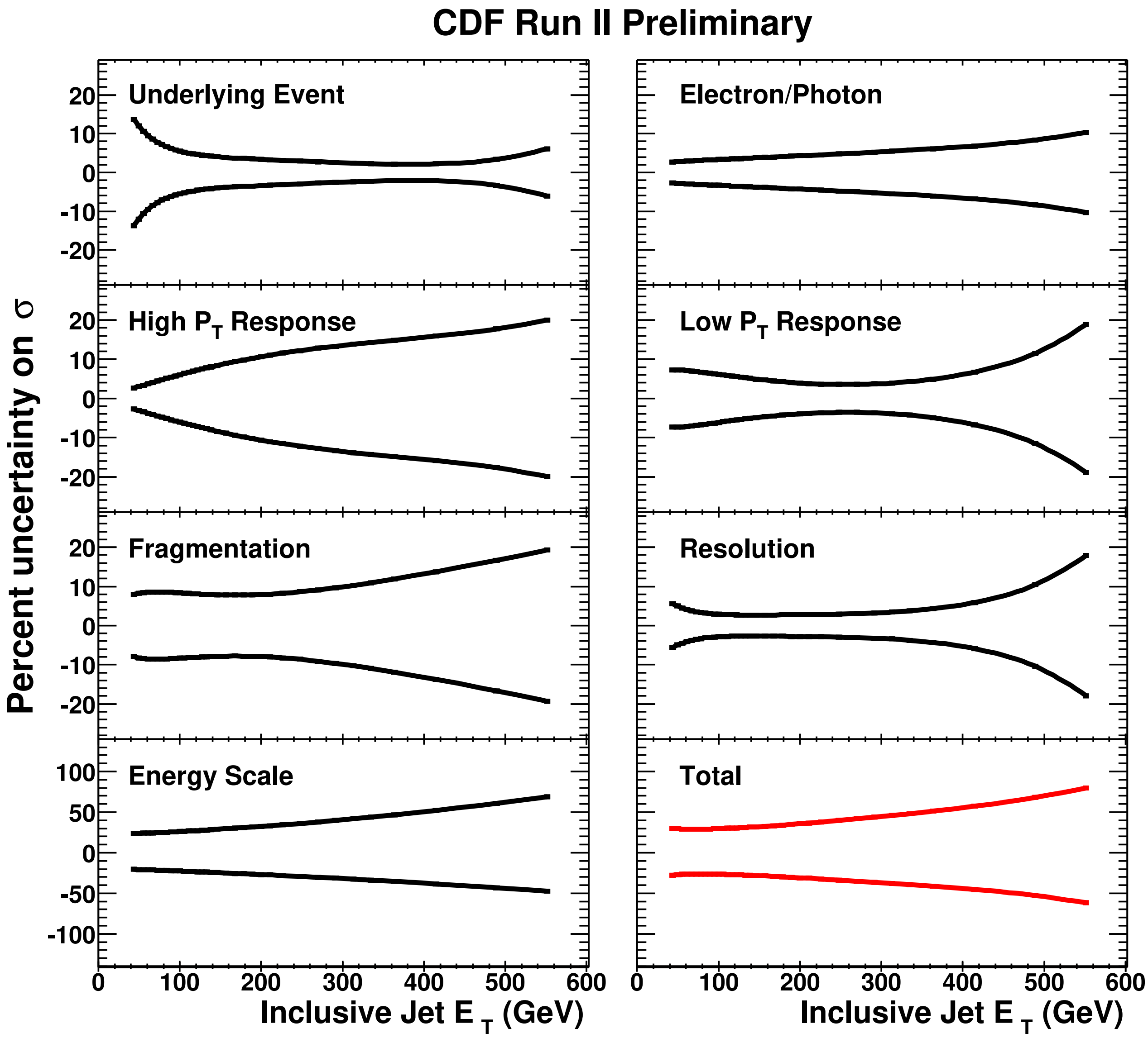

Figure 14: The percentage error on the corrected cross section resulting from the individual contributions to the total systematic error. The dominant uncertainty comes from the shift in energy scale.

The parameters of the physics functions determined for each source of systematic uncertainty are listed in Table 14. The one-sigma uncertainties on the cross section for each source are shown in Figure 14 as a percentage versus jet E_T. The dominant systematic uncertainty comes from the shift in energy scale, as shown in Figure 15.

Sys error	p_0	p_1	p_2	p_3	p_4	p_5	p_6
Nominal	0.23892E+06	–2.3859	4.6578	–5.0552	1.7446	–0.2070	7.0888
Ele/pho N	0.14922E+08	–4.5909	4.2562	–3.3789	0.9083	–0.0730	9.4803
Ele/pho P	0.11070E+08	–4.8078	5.0650	–4.0845	1.1628	–0.1072	8.9551
E scale N	0.26976E+06	–2.4170	4.5272	–5.0172	1.7746	–0.2191	6.5551
E scale P	0.68128E+06	–2.6910	4.5835	–4.9942	1.7748	–0.2239	4.4253
Frag N	0.94674E+07	–4.9981	5.5442	–4.4042	1.2491	–0.1164	8.4303
Frag P	0.36132E+06	–2.4681	4.5247	–5.0151	1.7763	–0.2183	6.7994
Hi p_T N	0.21768E+06	–2.2124	4.4980	–5.0352	1.7722	–0.2156	6.4929
Hi p_T P	0.19652E+06	–2.1737	4.4959	–5.0392	1.7699	–0.2166	6.0041
Lo p_T N	0.19367E+06	–2.1507	4.4985	–5.0392	1.7697	–0.2167	5.7238
Lo p_T P	0.23461E+06	–2.2652	4.4956	–5.0331	1.7737	–0.2149	7.1520
Res N	0.40779E+06	–2.4523	4.5214	–5.0179	1.7750	–0.2187	6.0437
Res P	0.70104E+07	–4.9984	5.7187	–4.5947	1.3312	–0.1283	8.9305
UE N	0.47090E+06	–2.3809	4.4818	–5.0336	1.7747	–0.2141	7.1747
UE P	0.40736E+07	–4.9159	5.6363	–4.3766	1.1988	–0.1038	9.4034

Table 14: The parameters of the physics function fits for different sources of systematic uncertainty.

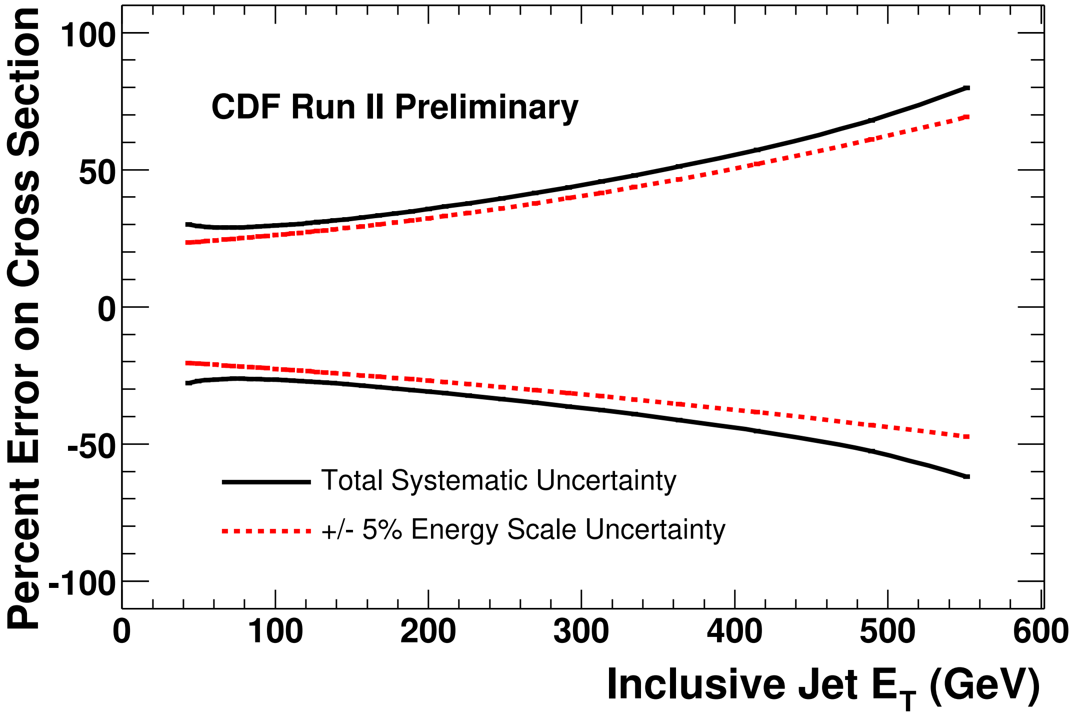

Figure 15: The percent error on the cross section measurement due to a 5% shift in the energy scale (inner band). The total systematic uncertainty is shown as the outer band.

8.1 Events at High E_T

The run and event numbers of the highest E_T jets are listed in Table 15.

Run	Event	N jets	E_{tot} (GeV)	$\widetilde{\not{E}_T}$	Uncorr E_T (GeV)	η_J
143257	276943	4	1027.4	0.4450	420.41	0.4063
151128	295868	5	1272.1	0.4678	518.05	0.1986
151128	295868	5	1272.1	0.4678	507.24	−0.5463
151555	1596656	4	1040.1	1.2083	427.63	0.1014
152507	1222318	6	1394.0	1.3615	607.50	0.4341
152507	1222318	6	1394.0	1.3615	569.10	−0.1930
153075	2273678	6	1254.9	0.6215	445.53	−0.6459
153075	2273678	6	1254.9	0.6215	432.38	0.5462
153447	4457374	4	1044.8	0.6061	421.70	−0.3696
153618	774625	2	927.6	4.5764	468.61	−0.5119
154861	916223	3	916.0	2.8971	432.28	0.0794
155345	3094590	4	1164.6	0.4588	439.67	0.0864
155364	72998	4	1227.3	0.4966	528.28	0.0120
155997	1270890	2	962.9	1.0748	435.58	0.2719
156116	942464	4	971.3	2.6651	424.20	−0.1306

Table 15: The run and event numbers of the highest-E_T jets.

9 Results and Comparisons to QCD Predictions

The raw cross section from the Run II data is compared to the Run I data on a log scale in Figure 16 and on a linear scale in Figure 17. The unsmeared Run II inclusive jet cross section is shown on a log scale in Figure 18, compared to NLO QCD predictions using the EKS program [10] with the CTEQ6.1M [4] PDF set. The EKS program is the standard NLO calculation that CDF has used in the past for evaluation of theoretical inclusive jet cross section predictions for comparison to data. In all calculations quoted in this note, EKS predictions use a renormalization and factorization scale equal to $E_T^{jet}/2$.

The CTEQ6.1M PDFs are an update to the published CTEQ6M PDFs, using a more accurate evaluation of the NLO jet cross sections in the global fitting process. (The differences between the CTEQ6.1M and CTEQ6M predictions are at the level of a few percent.) The CTEQ6.1M PDFs have incorporated all of the inclusive jet cross section data from Run I, and thus, along with the MRST2002 [11] PDFs, represent the most complete information available for Run II jet predictions. In addition, the CTEQ6.1M set of PDFs have available complete error information, which makes it

E_T low (GeV)	E_T high (GeV)	$< E_T >$ (GeV)	N events	Raw cross section (nb)
40	45	42	69288	42.19 ± 0.1603
45	50	47	37472	22.81 ± 0.1178
50	55	52	21588	13.13 ± 0.08939
55	60	57	13142	7.996 ± 0.06975
60	65	62	8069	4.91 ± 0.05466
65	70	67	5116	3.113 ± 0.04353
70	75	72	53975	2.103 ± 0.009052
75	80	77	36477	1.421 ± 0.007443
80	85	82	25694	1.002 ± 0.006249
85	90	87	18115	0.7061 ± 0.005246
90	95	92	12859	0.5011 ± 0.004419
95	100	97	23729	0.3714 ± 0.002411
100	105	102	17341	0.2714 ± 0.002061
105	110	107	12893	0.2018 ± 0.001777
110	115	112	9951	0.1557 ± 0.001561
115	120	117	7464	0.1168 ± 0.001352
120	125	122	5724	0.08956 ± 0.001184
125	130	127	4508	0.07052 ± 0.00105

Table 16: The raw cross section for events collected using the J20, J50 and J70 triggers.

E_T low (GeV)	E_T high (GeV)	$< E_T >$ (GeV)	N events	Raw cross section (nb)
130	140	134	50499	0.04931 ± 0.0002194
140	150	144	31410	0.03067 ± 0.000173
150	160	154	20157	0.01968 ± 0.0001386
160	170	164	13229	0.01292 ± 0.0001123
170	180	174	8811	0.008603 ± 9.165E–05
180	190	184	6027	0.005885 ± 7.58E–05
190	200	194	4218	0.004118 ± 6.341E–05
200	220	208	5003	0.002442 ± 3.453E–05
220	240	228	2391	0.001167 ± 2.387E–05
240	260	248	1298	0.0006337 ± 1.759E–05
260	280	269	683	0.0003334 ± 1.276E–05
280	300	288	400	0.0001953 ± 9.764E–06
300	320	309	215	0.000105 ± 7.158E–06
320	360	335	165	4.028E–05 ± 3.135E–06
360	440	387	69	8.421E–06 ± 1.014E–06
440	520	485	4	4.882E–07 ± 2.441E–07
520	620	568	3	2.929E–07 ± 1.691E–07

Table 17: The raw cross section for events collected using the J100 trigger.

E_T (GeV)	Cross section (nb)	E_T corr	Smear corr
43.7	$0.522 \times 10^{2} \pm 0.198 \times 10^{0}$	1.035	1.179
49.6	$0.274 \times 10^{2} \pm 0.142 \times 10^{0}$	1.050	1.144
55.5	$0.154 \times 10^{2} \pm 0.105 \times 10^{0}$	1.061	1.120
61.2	$0.926 \times 10^{1} \pm 0.808 \times 10^{-1}$	1.068	1.103
66.9	$0.563 \times 10^{1} \pm 0.626 \times 10^{-1}$	1.074	1.091
72.5	$0.354 \times 10^{1} \pm 0.495 \times 10^{-1}$	1.077	1.083
78.1	$0.238 \times 10^{1} \pm 0.102 \times 10^{-1}$	1.080	1.076
83.7	$0.160 \times 10^{1} \pm 0.837 \times 10^{-2}$	1.082	1.071
89.2	$0.112 \times 10^{1} \pm 0.700 \times 10^{-2}$	1.083	1.067
94.7	$0.789 \times 10^{0} \pm 0.586 \times 10^{-2}$	1.084	1.064
100.2	$0.559 \times 10^{0} \pm 0.493 \times 10^{-2}$	1.085	1.062
105.7	$0.413 \times 10^{0} \pm 0.268 \times 10^{-2}$	1.085	1.060
111.1	$0.301 \times 10^{0} \pm 0.229 \times 10^{-2}$	1.085	1.058
116.5	$0.224 \times 10^{0} \pm 0.197 \times 10^{-2}$	1.085	1.056
122.0	$0.172 \times 10^{0} \pm 0.173 \times 10^{-2}$	1.085	1.055
127.4	$0.129 \times 10^{0} \pm 0.150 \times 10^{-2}$	1.085	1.054
132.8	$0.990 \times 10^{-1} \pm 0.131 \times 10^{-2}$	1.085	1.053

Table 18: The unsmeared cross section for the J20, J50 and J70 triggers.

E_T (GeV)	Cross section (nb)	E_T corr	Smear corr
138.2	$0.779 \times 10^{-1} \pm 0.116 \times 10^{-2}$	1.085	1.052
146.0	$0.547 \times 10^{-1} \pm 0.243 \times 10^{-3}$	1.084	1.057
156.8	$0.340 \times 10^{-1} \pm 0.192 \times 10^{-3}$	1.084	1.055
167.6	$0.218 \times 10^{-1} \pm 0.153 \times 10^{-3}$	1.084	1.053
178.4	$0.143 \times 10^{-1} \pm 0.124 \times 10^{-3}$	1.083	1.051
189.2	$0.949 \times 10^{-2} \pm 0.101 \times 10^{-3}$	1.083	1.050
200.0	$0.649 \times 10^{-2} \pm 0.835 \times 10^{-4}$	1.083	1.050
210.8	$0.454 \times 10^{-2} \pm 0.699 \times 10^{-4}$	1.083	1.050
226.1	$0.273 \times 10^{-2} \pm 0.386 \times 10^{-4}$	1.083	1.066
247.9	$0.131 \times 10^{-2} \pm 0.268 \times 10^{-4}$	1.083	1.069
269.7	$0.716 \times 10^{-3} \pm 0.199 \times 10^{-4}$	1.083	1.076
291.5	$0.381 \times 10^{-3} \pm 0.146 \times 10^{-4}$	1.084	1.088
313.2	$0.227 \times 10^{-3} \pm 0.113 \times 10^{-4}$	1.084	1.106
334.8	$0.125 \times 10^{-3} \pm 0.850 \times 10^{-5}$	1.083	1.131
363.7	$0.517 \times 10^{-4} \pm 0.402 \times 10^{-5}$	1.082	1.222
415.1	$0.134 \times 10^{-4} \pm 0.161 \times 10^{-5}$	1.074	1.515
490.2	$0.910 \times 10^{-6} \pm 0.455 \times 10^{-6}$	1.048	1.775
552.4	$0.815 \times 10^{-6} \pm 0.471 \times 10^{-6}$	1.001	2.651

Table 19: The unsmeared cross section for the J100 trigger.

possible to calculate the PDF errors on the Run II jet cross section predictions (or on any CDF cross section, for that matter). The theoretical uncertainty on the Run II inclusive jet cross section due to PDFs is indicated in Figure 18; also indicated in the figure is the uncertainty band due to the 5% energy scale uncertainty. The 5% energy scale uncertainty is the dominant experimental systematic error.

In Figure 19, the same comparisons are also made on a linear scale. Here, the data are in good agreement with the NLO QCD predictions within the theoretical and experimental uncertainty bands. There is some indication of the data being below the theory at low E_T and somewhat above at higher E_T, but overall the agreement is good. It is important to point out that the CTEQ6.1M gluon already is "enhanced" at high x and so automatically leads to a larger prediction for the jet cross section than an older PDF such as CTEQ5M. The combined statistical power of the Run I inclusive jet cross section data of CDF and D0, and the fact that the data from both experiments prefer a larger gluon at high x, have led to this enhancement. For completeness, a comparison of a NLO QCD prediction using the CTEQ6.1M PDFs to the CDF inclusive jet cross section from Run I is shown in Figure 20 and the results for both Run I and Run II are shown in Figure 21. Note that the tendency for the data to be below the theory at low E_T is present here as well. The PDF uncertainties shown in Figure 19 may require some elaboration. The CTEQ6.1M global analysis has incorporated correlated systematic error information for all of the DIS (deep inelastic scattering), DY (Drell-Yan) and jet datasets included in the global fit, involving a total of almost 1900 data points. Twenty free parameters, corresponding to various terms in the expressions for the quark and gluon PDFs, were used in the global fit. As part of the global analysis, the Hessian error matrix (20×20, for the 20 free parameters) was calculated and diagonalized. The 20 eigenvectors so determined represent orthogonal directions in a PDF parameter space. The eigenvectors corresponding to the largest eigenvalues represent directions in the parameter space that are very well-determined, as for example the u and d valence quark distributions at moderate values of x. Eigenvectors corresponding to small eigenvalues represent poorly determined directions, as for example those exploring the behavior of the gluon distribution at large x. The CTEQ6.1M error PDFs correspond to excursions along each of the eigenvector directions that allow the total χ^2 for the global fit to increase by a $\delta\chi^2$ value of 100. Such an increase has been determined to represent a reasonable variation of the global χ^2, corresponding to something like a 90% confidence level. There are 20 eigenvectors, with asymmetric excursions possible along the "+" and "–" directions, leading to a total of 40 error PDFs. The dominant PDF uncertainty for the inclusive jet cross section comes from two eigenvectors, +15 and –15 (*i.e.* the two directions for the 15th largest eigenvalue), a direction that probes the behavior of the high x gluon. In fact, as one can observe in Figure 19, there is still a wide range of uncertainty remaining for jet cross sections at high E_T. The full Run II dataset from CDF will help to reduce this uncertainty.

As mentioned previously, the increase in the center-of-mass energy from Run I to Run II has a fairly large effect on the high E_T jet cross section. It is instructive to

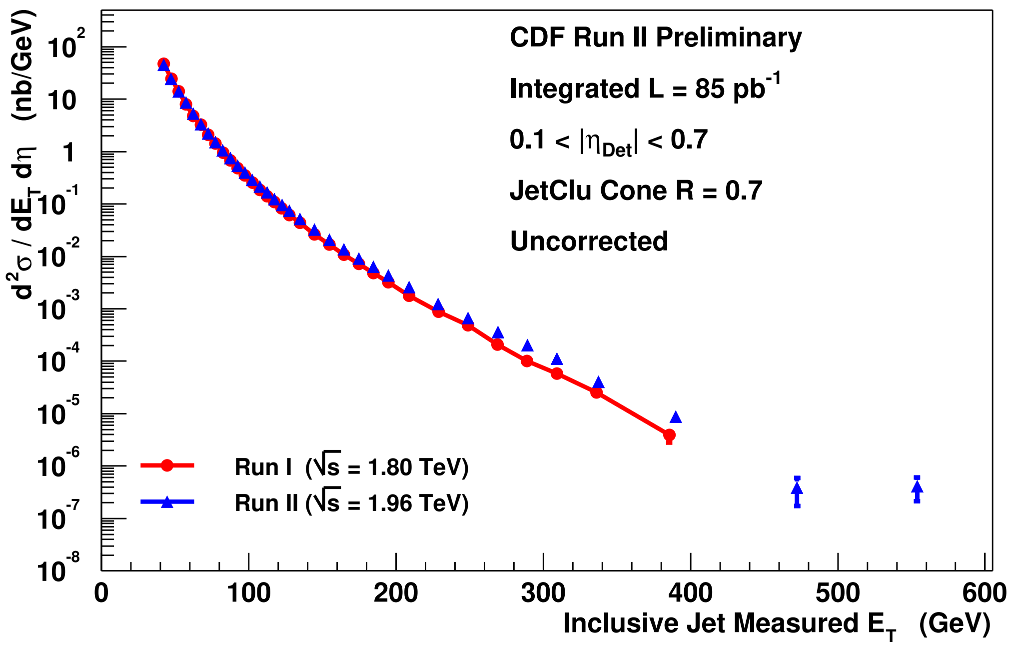

Figure 16: The Run II raw data compared to the Run I raw data.

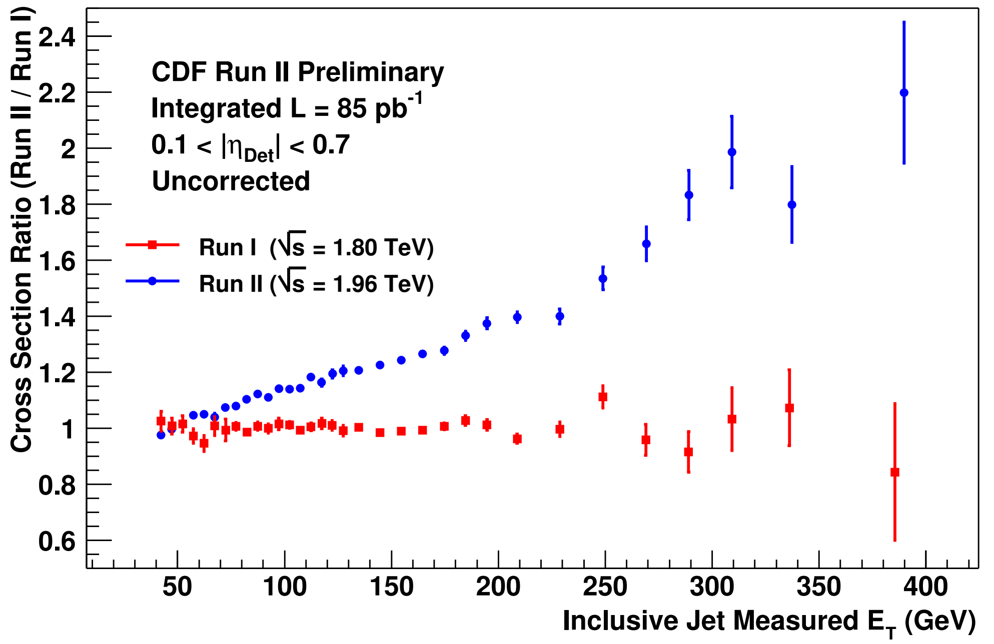

Figure 17: The Run II raw data compared to the Run I raw data.

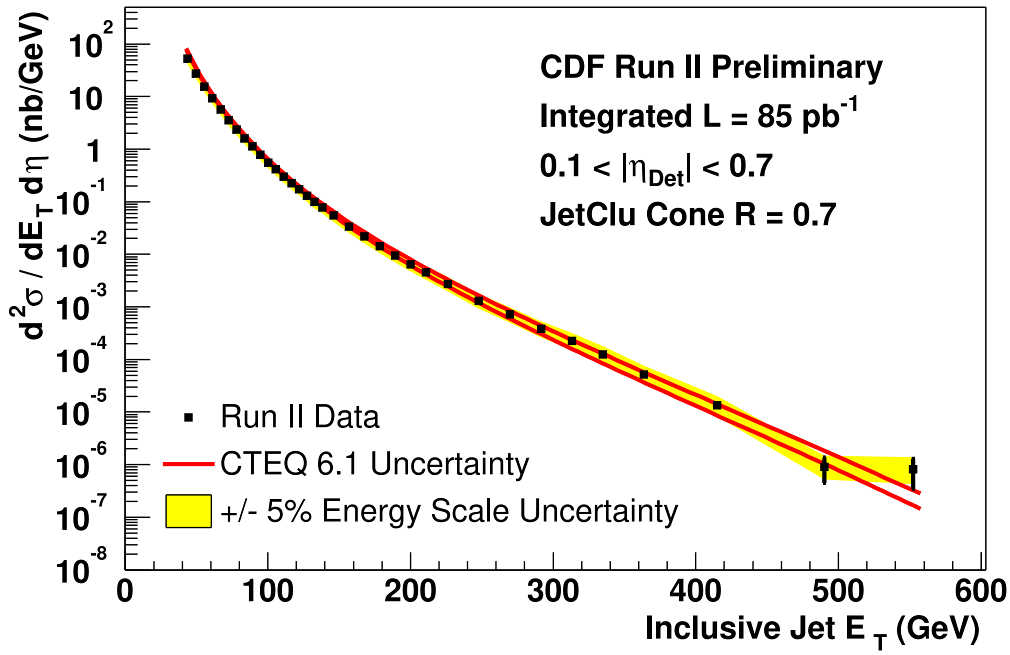

Figure 18: The Run II data compared to the NLO QCD predictions using CTEQ 6.1. The error band shows the change in the cross section due to the 5% energy scale shift.

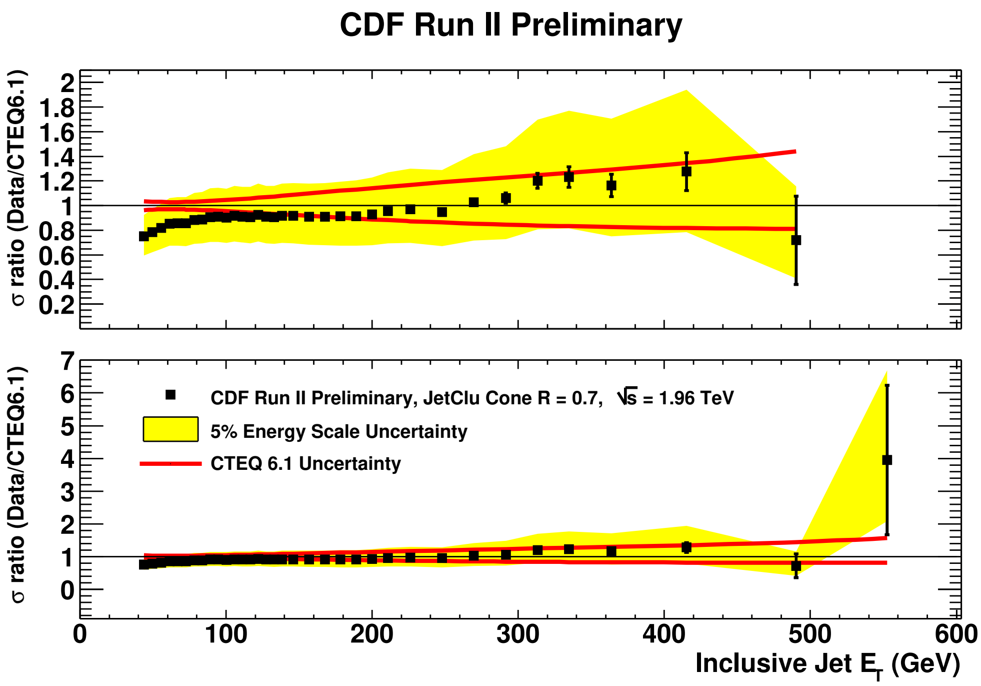

Figure 19: The data divided by the theory using CTEQ 6.1.

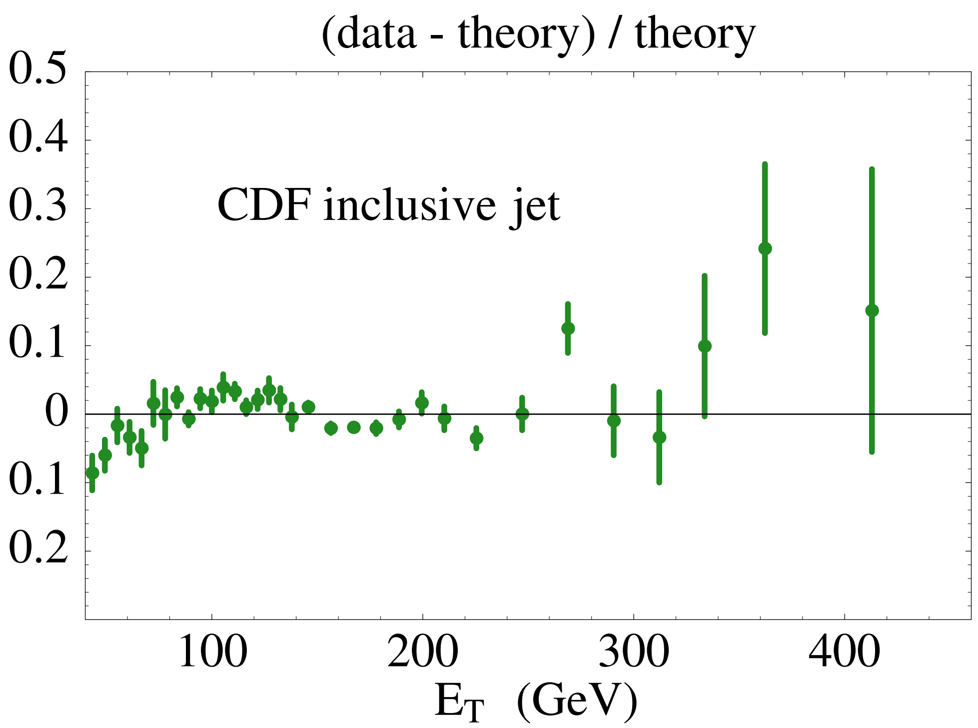

Figure 20: The Run I data compared to NLO theory using CTEQ6.1.

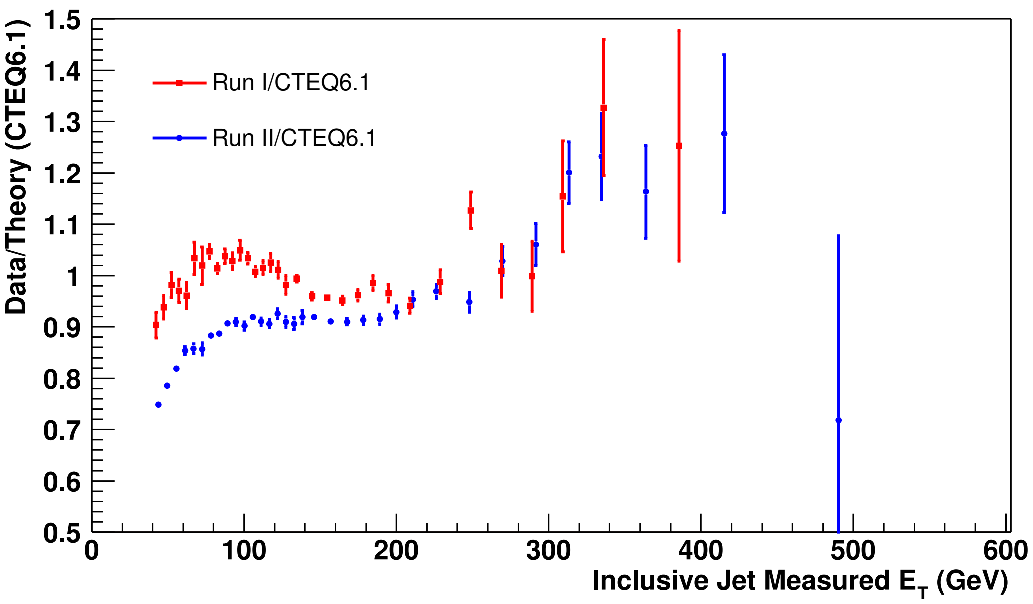

Figure 21: The Run I and Run II data compared to the predictions of CTEQ6.1 PDF.

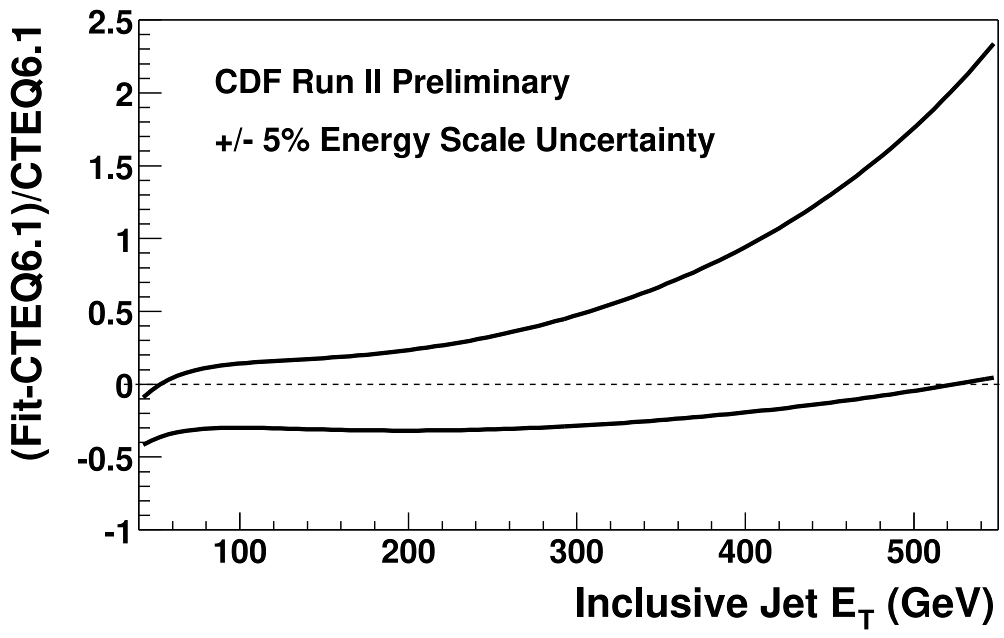

Figure 22: The 5% energy scale error band centered around the fit to the data and compared to CTEQ 6.1.

examine the ratio of the Run II jet cross section to the Run I cross section as a function of the jet transverse energy. Systematic errors, both theoretical and experimental, should mostly cancel in the ratio. This is also an indirect way of checking whether the 4.2% increase adopted for the jet energy scale is warranted.

The ratio of the two jet cross sections is shown in Figure 24, along with the systematic error bands due to the PDF uncertainty and the experimental uncertainty due to the energy scale. The data ratio is seen to be lower than the theoretical expectations by about 20% at low E_T and it rises somewhat faster than expected. The agreement is good for E_T values larger than 200 GeV. A more complete analysis taking into account the systematic errors will be required to quantify the significance of this behavior.

References

[1] H.L. Lai *et al.*, "Improved Parton Distributions from Global Analysis of Recent Deep Inelastic Scattering and Inclusive Jet Data," Phys. Rev. D **55** (1997) 1280–1296, (hep-ph/9606399).

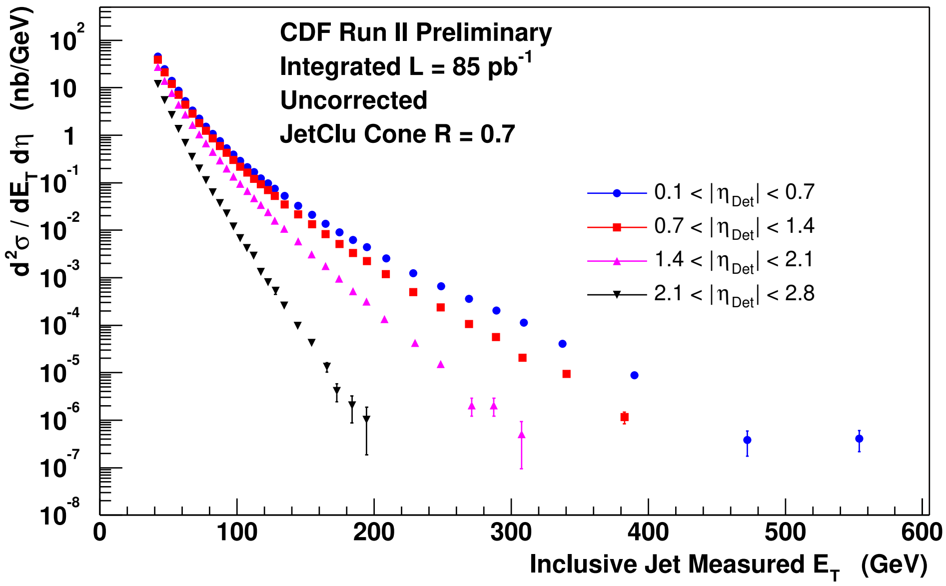

Figure 23: The inclusive jet cross section for different η_D regions.

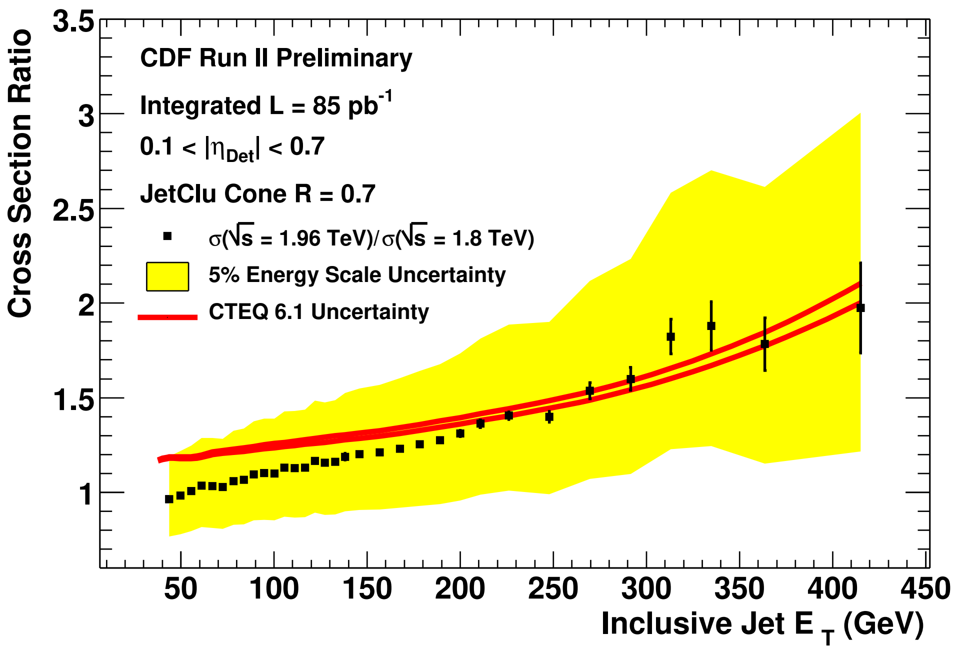

Figure 24: The cross section ratio of the Run II data points over the Run I fit to the data (blue), compared to that expected from theory (green). The theoretical ratio is displayed as a band reflecting the systematic uncertainty due to PDFs. The ratio of the Run I data points over the Run I fit to the data is shown in red.

[2] H.L. Lai *et al.*, "Global QCD Analysis of Parton Structure of the Nucleon: CTEQ5 Parton Distributions," Eur. Phys. J. C12 (2000) 375–392, (hep-ph/9903282).

[3] J. Pumplin *et al.*, "New Generation of Parton Distributions with Uncertainties from Global QCD Analysis," JHEP 0207 (2002) 012, (hep-ph/0201195).

[4] D. Stump *et al.*, "Inclusive Jet Production, Parton Distributions, and the Search for New Physics," hep-ph/0303013.

[5] T. Affolder *et al.*, "Measurement of the Inclusive Jet Cross Section in $p\overline{p}$ Collisions at $\sqrt{s} = 1.8$ TeV," Phys. Rev. D **64** (2001), 032001.

[6] W.K. Sakumoto and A. Hocker, "Event $|Z_{\rm vtx}| \leq 60$ cm Cut Efficiency for Run II," CDF/ANAL/ELECTROWEAK/CDFR/6331.

[7] I. Gorelov, "A Background Filter for QCD Triggers with the Hadron Calorimeter TDC System," CDF/ANAL/JET/CDFR/6145.

[8] G. Latino, "Jet EM Fraction Studies: RunII-RunI Comparison on γ-Jet Data," CDF/ANAL/JET/CDFR/6152.

[9] R. Harris, F. Chlebana, "Search for New Particles Decaying to Dijets in Run 2," CDF/ANAL/EXOTIC/CDFR/6248.

[10] S.D. Ellis, Z. Kunszt, D.E. Soper, "The One Jet Inclusive Cross-Section at Order α_s^3: Quarks and Gluons," Phys. Rev. Lett. **64**, 2121 (1990).

[11] A.D. Martin, R.G. Roberts, W.J. Stirling, R.S. Thorne, "Uncertainties of Predictions from Parton Distributions I: Experimental Errors," hep-ph/0211080.